

On the Development and Evaluation of Spatial-Domain Green's Functions for Multilayered Structures With Conductive Sheets

Ioannis D. Koufogiannis, *Member, IEEE*, Michael Mattes, *Member, IEEE*, and Juan R. Mosig, *Fellow, IEEE*

Abstract—This work focuses on Green's functions (GFs) of planar multilayered structures that may include an arbitrary number of conductive sheets. The spectral-domain GFs are derived through an automatized strategy based on the propagator matrix technique, while the spatial-domain counterparts are evaluated using a novel, efficient, and error controlled numerical method. All of the procedures remain general in order to accommodate for the tensorial nature of the surface conductivity of the sheets. Numerical examples of GFs for the mixed potential integral equation method are provided, validating the proposed algorithms.

Index Terms—Conductive interfaces, Green's functions, integral equations, MPIE, multilayered structures, tensorial conductivity.

I. INTRODUCTION

MICROWAVE and RF components, based on planar multilayered structures, can be integrated easily within printed circuits providing a cost effective performance. Recent developments in the fields of transformation optics [1], plasmonic antennas [2], strong light-matter interaction [3], or solar antennas [4] include the addition of very thin metallizations among the stacked dielectric layers, forming conductive interfaces, in order to achieve the desired electromagnetic performance. Frequently, these thin metallizations can be assumed to extend to infinity in the lateral directions if their size is much larger than the wavelength and edge effects can be neglected, or if the surface waves attenuate very fast, as in the case of plasmons in graphene sheets. The classical numerical EM algorithms, which usually require an explicit definition of the thickness of the conductive sheets [5], are able to handle these structures only as a limiting case with thickness tending to zero. Therefore, they show very poor performance in simulating such structures and have to be readdressed.

Manuscript received July 15, 2014; revised October 17, 2014, November 20, 2014; accepted November 20, 2014. Date of publication December 18, 2014; date of current version December 31, 2014. This work was supported in part by the European COST Action IC-1102 VISTA. This paper is an expanded version from the IEEE MTT-S International Conference on Numerical Electromagnetic Modeling and Optimization for RF, Microwave, and Terahertz Applications, Pavia, Italy, May 14–16, 2014.

The authors are with the Laboratory of Electromagnetics and Acoustics (LEMA), Ecole Polytechnique Fédérale de Lausanne (EPFL), Lausanne 1015, Switzerland (e-mail: ioannis.koufogiannis@epfl.ch).

Color versions of one or more of the figures in this paper are available online at <http://ieeexplore.ieee.org>.

Digital Object Identifier 10.1109/TMTT.2014.2375829

Among various computational EM techniques, an integral equation formulation linearized through a Method of Moments procedure (IE-MoM) offers competitive performance for modeling planar multilayered structures. Plenty of IE-MoM formulations have been proposed in literature, with the most popular including the one based on the electric field (EFIE), on the magnetic field (MFIE), or on the combination of both electric and magnetic field equations into a combined field equation (CFIE) and finally the mixed potential integral equation (MPIE). Specifically, MPIE receives special attention, as it calls only for the evaluation of $1/R$ singularities of the scalar and vector potentials [5] and will be specially referenced throughout the current work.

One of the cornerstones of all of the IE based methods is the derivation of the relevant Green's functions (GFs), which is the focus of the current work. In general, this is a tedious and time-consuming task. In the specific case of a multilayered structure that is transversally invariant, the GFs can be derived through their closed-form spectral-domain counterparts by applying a double inverse Fourier transform (IFT).

Different techniques have been deployed for the numerical evaluation of the spatial-domain GFs. Generally speaking, they can be divided into two large families. The methods that belong to the first family approximate the spectral-domain GF through appropriate functions, e.g., a sum of spectral-domain discrete images or rational functions, whose IFT is either analytical or much simplified. Representative examples of this idea can be found in [6]–[11], to mention only a few. The extremely fast evaluation of the spatial-domain GFs through these methods comes at the cost of limited accuracy, as a result of the approximation of the spectral-domain GFs. Most of the cited papers invent clever ways to improve the numerical accuracy of the calculations, yet most of the performed experiments hardly reach single precision accuracy. The second family includes methods that focus on the numerical integration of the IFT integrals, which is a computationally expensive task, but machine precision results can be achieved in practice. Investigations in this direction can be found in [5], [12]–[16] and also in this work.

In applications where fast computations with a rough accuracy of some significant digits are required, methods of the first family should be selected. If the accuracy of the results needs to be guaranteed or machine precision calculations are required in order to avoid propagation errors in further calculations, then more computational resources have to be deployed, and methods from the second family should be chosen. Typical

examples, where a lack of accuracy results in destructive propagation errors, is the inversion of ill-conditioned MoM matrices or interpolation of spatial-domain GFs for fast filling of the MoM reaction integrals [17]–[19].

The present work serves as an extension of the basic ideas presented in [20]. A robust way for deriving the spectral domain GFs of multilayered structures, including zero-thickness sheets with tensorial surface conductivity—their lateral dimensions being infinite, is proposed. The planar structures with conductive sheets that are analyzed in the literature usually include only one or two such sheets and the GFs can be manually derived. Utilizing the methods hereby described, spectral-domain GFs for complicated structures with multiple layers and sheets are at hand.

Additionally, a novel numerical integration routine based on advanced quadrature rules is developed for calculating the spatial-domain GFs with controlled and high accuracy. Extended details on the mathematical developments, an implementation strategy that boosts the performance of the proposed technique, have been added. Last but not least, additional numerical examples are presented, where comparison with other numerical methods is shown, validating the discussed method.

This paper is organized as follows. In Section II, a generalized procedure for deriving the spectral-domain GFs for the EM fields and the mixed potentials GFs is developed. The methodology has been extended to take into account multilayered structures with arbitrary numbers of conductive sheets, both of scalar and tensorial nature. Having at hand the spectral-domain GFs, an efficient and novel numerical strategy for evaluating their spatial-domain counterparts is presented in Section III, followed by the algorithmic details of the proposed approach in Section IV. The described technique offers controllable accuracy up to machine precision while simultaneously outperforming traditional methods in terms of computational time. This is possible by utilizing a powerful numerical integration method, namely the Double Exponential (DE) rule, which is enhanced and fine tuned for the specific numerical problems. The details of this algorithm are analyzed in Section V. Finally, numerical results for technologically interesting structures and comparisons against alternative numerical techniques are shown in Section VI, validating the performance and robustness of the methods presented within this contribution.

II. DEVELOPMENT OF SPECTRAL-DOMAIN GREEN'S FUNCTIONS

In case of an arbitrary multilayered structure like the one in Fig. 1, the GFs need to be derived. A usual approach is to solve the equivalent transmission line systems [21]. Since in the following sections we are going to introduce conductive sheets and their corresponding boundary conditions, we hereby choose a method based on connecting the normal components of the EM fields through the different interfaces. This method is usually called the Propagator Matrix technique [5] and was initially developed for dielectric interfaces only.

The Propagator Matrix technique [5] is a powerful technique for deriving spectral domain GFs of multilayered structures in a general way. As its name reveals, it propagates the electric and magnetic fields created by electric and magnetic sources

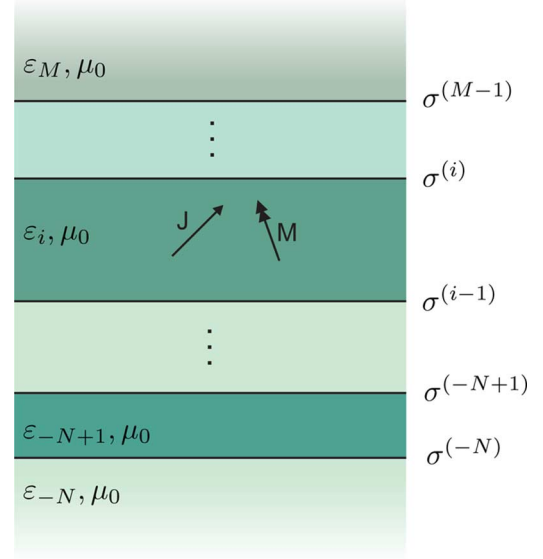


Fig. 1. General multilayered structure with dielectric layers and conductive interfaces.

through the different dielectric layers of the structure upon the terminating interfaces, where appropriate boundary conditions are imposed. The terminating boundary conditions can be chosen among Sommerfeld radiation condition, PEC, PMC, or surface impedance condition. The original development of the Propagator Matrix technique was targeting structures with multiple dielectric layers. Recent advances in material science used in multilayered microwave and THz components as well as the introduction of very thin, up to nanoscale- or even atom-level, conductive layers calls for the enhancement of this technique. Therefore, an appropriate boundary condition that connects the normal components of the electric and magnetic fields when a conductive sheet is present is hereby derived by enforcing the appropriate boundary conditions for the tangential fields. This results in the following propagation block:

$$\begin{bmatrix} \tilde{G}_{EJi+1}^{zn(i)} \\ \frac{\partial \tilde{G}_{EJi+1}^{zn(i)}}{\partial z} \\ \tilde{G}_{HJi+1}^{zn(i)} \\ \frac{\partial \tilde{G}_{HJi+1}^{zn(i)}}{\partial z} \end{bmatrix} = \begin{bmatrix} \frac{\varepsilon_i}{\varepsilon_{i+1}} & \frac{-j\sigma_{uu}^{(i)}}{\omega\varepsilon_{i+1}} & \frac{\mu_0\sigma_{uv}^{(i)}}{\varepsilon_{i+1}} & 0 \\ 0 & 1 & 0 & 0 \\ 0 & 0 & 1 & 0 \\ 0 & \sigma_{vu}^{(i)} & j\omega\mu_0\sigma_{vv}^{(i)} & 1 \end{bmatrix} \begin{bmatrix} \tilde{G}_{EJi}^{zn(i)} \\ \frac{\partial \tilde{G}_{EJi}^{zn(i)}}{\partial z} \\ \tilde{G}_{HJi}^{zn(i)} \\ \frac{\partial \tilde{G}_{HJi}^{zn(i)}}{\partial z} \end{bmatrix} \quad (1)$$

which connects the normal components of the fields in the layer i below the conductive interface (i) with the ones above it in the layer $i + 1$. The excitation is an n directed electric dipole, $n \in \{x, y, z\}$. Magnetic currents can also be included in the current formulation in a similar manner. The conductivity of the interface (i) can be tensorial, i.e., $\vec{\sigma} = \sigma_{uu}\hat{u}\hat{u} + \sigma_{uv}\hat{u}\hat{v} + \sigma_{vu}\hat{v}\hat{u} + \sigma_{vv}\hat{v}\hat{v}$, where \hat{u} and \hat{v} are the rotated spectral-domain coordinates [22], which reduces to the scalar case if $\sigma_{uu} = \sigma_{vv} = \sigma$ and $\sigma_{uv} = \sigma_{vu} = 0$. From (1), it becomes obvious that, in the case of an interface with scalar conductivity, the TM and TE components of the EM fields remain uncoupled, which is no longer the case if the conductivity is tensorial.

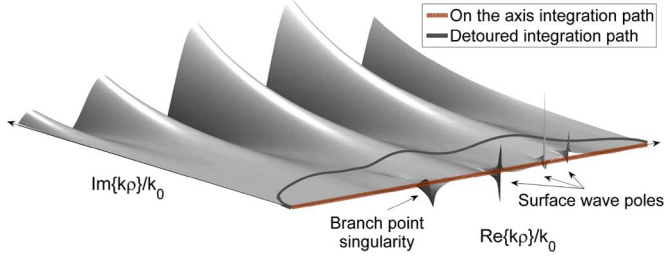


Fig. 2. Integrant of a typical Sommerfeld integral, with the branch point and three surface wave poles visible. The common off-the-axis, detoured path and the proposed on-the-axis integration path are indicated.

The connection of the GFs for the EM fields with the GFs for the vector and scalar potential in the spectral domain can be resolved in a unique way by enforcing the Lorenz Gauge and the Sommerfeld choice for the potentials [22]–[24]. Consequently, the spectral-domain GFs for a MPIE become available as shown in [23]–[25], and, in order to serve as input for a IE-MoM code, their spatial-domain counterparts have to be efficiently calculated. This task is discussed in detail in Section III.

III. EVALUATION OF SOMMERFELD INTEGRALS

The spatial-domain GFs are connected to the spectral domain ones through the generalized Sommerfeld integrals [26]

$$G(\rho, z, z') = S_n[\tilde{G}] \triangleq \int_0^\infty J_n(k_\rho \rho) k_\rho^{n+1} \tilde{G}(k_\rho, z, z') dk_\rho \quad (2)$$

where J_n is the n th-order Bessel function of the first kind, ρ is the horizontal distance between source and observation point, and z and z' are their vertical positions, respectively. \tilde{G} can be chosen among the components of the spectral-domain GFs either for the fields or for the potentials, which are available in closed form based on the analysis presented in Section II. Finally, the order n of the Bessel function is chosen depending on the rotational properties of \tilde{G} in the complex plane based on Sommerfeld identities [27].

The numerical evaluation of Sommerfeld integrals (2) becomes nontrivial due to:

- the semi-infinite domain of integration combined with the fast oscillations due to the presence of the Bessel function;
- the presence of the branch point, where the higher order derivatives of the integrand are not bounded;
- possible surface waves poles the spectral-domain GFs \tilde{G} may introduce.

Traditionally, the integration path is deformed in the complex k_ρ -plane in order to avoid the branch point and the singularities. However, the deformed path suffers from high oscillations due to the imaginary part of the argument of the Bessel function, as shown in Fig. 2. An optimal deformed path that minimizes the effect of the poles and the oscillations of the Bessel function is found to be the elliptical contour [28]. However, it is clear that, if the position of the singular points vary from very close to the branch point to very far away from it, which is a typical situation if surface plasmon polaritons (SPPs) are propagating on a graphene layer at THz frequencies [29], then the deformed path integration becomes incredibly inefficient.

As an alternative and in order to improve the efficiency and the accuracy of the numerical evaluation of (2), an integration path on the real axis is hereby proposed. Such a scheme should be able to cope with the poles of the GF in the complex plane and the branch point singularities.

As a first step, the poles of \tilde{G} have to be identified, extracted, and added back analytically in the spatial domain. The identification of the location of the poles is not always easy, especially if plasmon modes are propagating. Fortunately, powerful methods have been developed that can be hereby employed [30]–[34]. It has to be mentioned that this task is performed only once in the beginning of the EM analysis for each frequency, regardless of the position of the source and the observation points.

As the poles $k_{\rho i}$, including surface wave and plasmon ones— i pointing to each one of the N_p poles of the multi-layered structure at the operating frequency—appear in pairs in the complex plane, each pair $\pm k_{\rho i}$ should be subtracted. Moreover, another pair of spurious, nonexistent poles $\pm j k_{\rho i}$ is also subtracted, since it has been shown that such an action improves the convergence of the remaining integrals [35], [36]. Alternatively, singularity subtraction techniques improving the spectral behavior of the integrand can also be used [37].

Finally, the part subtracted from the spectral-domain GF \tilde{G}^p can be written as

$$\tilde{G}^p(k_\rho) = \sum_{i=1}^{N_p} \left(\frac{2R_i k_\rho}{k_\rho^2 - k_{\rho i}^2} - \frac{2R_i k_\rho}{k_\rho^2 + k_{\rho i}^2} \right) = \sum_{i=1}^{N_p} \frac{4R_i k_\rho^3}{k_\rho^4 - k_{\rho i}^4}. \quad (3)$$

The residuals R_i are calculated by integrating in the complex plane the GF \tilde{G} over a closed contour that includes only the corresponding pole $k_{\rho i}$. The integration path is usually chosen to be a circle due to the easiness in its parametrization, therefore the residuals of each pole can be calculated through

$$R_i = \frac{1}{2\pi} \int_0^{2\pi} \tilde{G}(k_\rho) \alpha e^{j\phi} d\phi \quad (4)$$

using standard integration routines, where $k_\rho = k_{\rho i} + \alpha e^{j\phi}$ and the radius α is chosen so that no other pole is included in the closed integration domain.

Having identified the position of the poles and the values of the residuals, the transformation of (3) to the spatial domain can be performed analytically using the identities

$$\begin{aligned} S_0\{\tilde{G}^p\} &= \int_0^\infty \tilde{G}^p(k_\rho) J_0(k_\rho \rho) k_\rho dk_\rho \\ &= - \sum_{i=1}^{N_p} k_{\rho i} R_i \left(j\pi H_0^{(2)}(k_{\rho i} \rho) + 2K_0(k_{\rho i} \rho) \right) \end{aligned} \quad (5)$$

$$\begin{aligned} S_1\{\tilde{G}^p\} &= \int_0^\infty \tilde{G}^p(k_\rho) J_1(k_\rho \rho) k_\rho^2 dk_\rho \\ &= - \sum_{i=1}^{N_p} k_{\rho i}^2 R_i \left(j\pi H_1^{(2)}(k_{\rho i} \rho) + 2K_1(k_{\rho i} \rho) \right) \end{aligned} \quad (6)$$

for the generalized Sommerfeld integrals S_0 and S_1 , respectively, where K_n is the modified Bessel function of order n [27].

The remainder of the GF $\tilde{G}^{np} = \tilde{G} - \tilde{G}^p$ does not include any poles, meaning that the pole extraction has already been

performed and the remaining branch point irregularity has to be treated.

In the next step, the integration domain is split into two parts $\mathcal{S}_n = \mathcal{I}_n + \mathcal{T}_n$, due to the nature of the kernel of the Sommerfeld integral. The first part includes only the branch point(s)

$$\mathcal{I}_n \left\{ \tilde{G}^{np}(k_\rho; z|z') \right\} = \int_0^{\xi_0} \tilde{G}^{np}(k_\rho; z|z') J_n(k_\rho \rho) k_\rho^{n+1} dk_\rho. \quad (7)$$

The upper limit ξ_0 is chosen such that no branch points are present in the remaining integrand for values $\text{Re}\{k_\rho\} > \xi_0$, which is

$$\mathcal{T}_n \left\{ \tilde{G}^{np}(k_\rho; z|z') \right\} = \int_{\xi_0}^{\infty} \tilde{G}^{np}(k_\rho; z|z') J_n(k_\rho \rho) k_\rho^{n+1} dk_\rho \quad (8)$$

This is called the tail of the Sommerfeld integral and comprises the high oscillations of the remaining singularity-free semi-infinite domain.

The choice of the separation point between the first part and the tail of the Sommerfeld integral ξ_0 is not so crucial due to the absence of the poles. However, it should be chosen relatively far away from $k_\rho = k$ so that the effect of the branch point will already be weakened before the integration of the tail begins. On the other hand, especially for large arguments of the horizontal separation ρ , the oscillations of the Bessel function are present even around $k_\rho = k < \xi_0$, in which case it is more efficient to choose ξ_0 closer to the branch point in order to take advantage of the special algorithms for the oscillating integrands.

The tail of the Sommerfeld integral is numerically evaluated through the Weighted Averages (WA) technique [13], whereas the remaining singularity-free first part can be integrated efficiently only if the branch point is properly treated. As the higher order derivatives of \tilde{G} are not bounded [38] at the branch point, standard quadrature rules fail. This difficulty can be overcome by employing advanced quadrature rules, that are able to handle such singularities. In the current work, the Double Exponential rule (DE) [39] is used, enhanced with an error estimator [40] that guarantees the accuracy of the numerical results. Finally, if all of the methods presented in Sections III–V are properly combined, the spatial-domain GFS for the scalar and vector potential of multilayered structures can be evaluated, as shown in Section VI.

IV. NUMERICAL EVALUATION OF THE FIRST PART OF SIS

Focusing on the numerical techniques, the irregular behavior of (7) at the branch point $k_\rho = k$ calls for a further split of the integration domain resulting into two integrals, with both of them being singular only at their common end-point $k_\rho = k$ as follows:

$$\mathcal{I}_n = \mathcal{I}_{n,a} + \mathcal{I}_{n,b} \quad (9)$$

where

$$\mathcal{I}_{n,a} = \int_0^k \tilde{G}^{np}(k_\rho) J_n(k_\rho \rho) k_\rho^{n+1} dk_\rho \quad (10)$$

$$\mathcal{I}_{n,b} = \int_k^{\xi_0} \tilde{G}^{np}(k_\rho) J_n(k_\rho \rho) k_\rho^{n+1} dk_\rho. \quad (11)$$

It should be pointed out that \tilde{G}^{np} explicitly includes the term $k_z = \sqrt{k^2 - k_\rho^2}$ and can be rewritten as

$$\tilde{G}^{np}(k_\rho) = \tilde{G}^{np}(k_\rho, k_z(k_\rho)). \quad (12)$$

The first-order derivative of (12) is

$$\frac{\partial \tilde{G}^{np}(k_\rho)}{\partial k_\rho} = \frac{\partial \tilde{G}^{np}(k_\rho, k_z)}{\partial k_z} \frac{\partial k_z}{\partial k_\rho} + \frac{\partial \tilde{G}^{np}(k_\rho, k_z)}{\partial k_\rho} \quad (13)$$

which obviously is unbounded for $k_\rho = k$; the same for all the higher order ones. This is the reason why special quadrature routines that are able to handle endpoint singularities should be used for the numerical integration of (10) and (11). Among them, the Double Exponential (DE) rule is chosen, as it is considered to be one of the most efficient routines for this purpose and will be discussed in detail in Section V.

As most of the quadrature rules, including the DE one, are defined over the $[-1, 1]$ integration domain, a suitable change of variables in $\mathcal{I}_{n,a}$ and $\mathcal{I}_{n,b}$ allows us to rewrite (10) and (11), respectively, as

$$\mathcal{I}_{n,a} = \int_{-1}^1 \tilde{G}^{np}(k_{\rho,a}(x), k_{z,a}(x)) J_n(k_{\rho,a}(x) \rho) \frac{k}{2} k_{\rho,a}^{n+1}(x) dx \quad (14)$$

$$\mathcal{I}_{n,b} = \int_{-1}^1 \tilde{G}^{np}(k_{\rho,b}(x), k_{z,b}(x)) J_n(k_{\rho,b}(x) \rho) \frac{\xi_0 - k}{2} k_{\rho,b}^{n+1}(x) dx \quad (15)$$

where

$$k_{\rho,a}(x) \rightarrow \frac{k}{2}(1+x) \quad (16)$$

$$k_{z,a}(x) \rightarrow \frac{k}{2}\sqrt{x+3}\sqrt{-x+1} = \frac{k}{2}\sqrt{x+3}\sqrt{H} \quad (17)$$

$$k_{\rho,b}(x) \rightarrow \frac{\xi_0 - k}{2} \left(x + \frac{\xi_0 + k}{\xi_0 - k} \right) \quad (18)$$

$$k_{z,b}(x) \rightarrow j \frac{\xi_0 - k}{2} \sqrt{x + \frac{\xi_0 + 3k}{\xi_0 - k}} \sqrt{1+x} \\ = j \frac{\xi_0 - k}{2} \sqrt{x + \frac{\xi_0 + 3k}{\xi_0 - k}} \sqrt{-10000fil}. \quad (19)$$

The binomials $-10000fil = 1+x$ and $H = 1-x$ have to be identified in (17) and (19), as they require special numerical treatment as shown in Section V.

The current development assumes a single branch point, which is the case for a multilayered structure backed on the one

side and radiating on the other one. All of these calculations can be easily generalized to the cases where two separated branch points are present, as in the case of a graphene sheet separating two different semi-infinite media.

V. DOUBLE EXPONENTIAL (DE) QUADRATURE RULE

The main integration tool that is utilized in the presented method is the DE quadrature rule [39]. DE targets integrals with end-point singularities, and details of the implementation can be found in [40]. The DE rule is based on a transformation function $\phi(t)$, which is carefully chosen in order to impose asymptotically a double exponential decay on the transformed integrand at both end-points

$$I_f = \int_{-1}^1 f(x) dx = \int_{-\infty}^{\infty} g(t) dt = \int_{-\infty}^{\infty} f(\phi(t)) \phi'(t) dt. \quad (20)$$

The optimal choice for the sampling of (20) is the trapezoidal rule [41], and the resulting infinite series is then truncated as follows:

$$I_f \approx \sum_{m=-n}^n f(x_m) w_m = \sum_{m=-n}^n f(\phi(mh)) \phi'(mh) h. \quad (21)$$

Fine tuning of the DE rule is possible through the discretization step h and the number of sampling points n . If they are properly chosen so that no underflow or overflow calculations occur, then up-to-machine-precision results can be obtained [38], [42], [43]. In this work, the original DE transformation found in [39] is replaced by a modified one, as the last one provides faster convergence to the desired accuracy [44]. This transformation is shown in

$$x = \phi(t) = \tanh(\sinh(t)). \quad (22)$$

The binomials $-10000fil = 1 + x$ and $H = 1 - x$ have to be identified in the integrand function $f(x)$, as done in (17) and (19), and be precomputed through

$$\begin{aligned} -10000fil = 1 + x &= \frac{\exp(\sinh(t))}{\cosh(\sinh(t))} \\ H = 1 - x &= \frac{\exp(-\sinh(t))}{\cosh(\sinh(t))} \end{aligned} \quad (23)$$

in order to overcome large round-off errors [40], [42].

Towards developing an efficient numerical tool for handling Sommerfeld integrals, the DE rule is enhanced with two additional utilities, adaptivity and error estimation. The first one is important because it reuses computations already performed, while the second one guarantees the accuracy of the calculated results. Both properties are discussed in the following subsections.

A. Implementation of Adaptive DE

The DE rule (21), (22), if discretized properly, can be enhanced to perform as an adaptive quadrature, that is a highly desirable property for modern quadrature rules. If, in each step, the sampling distance h is halved, then, at level N , the DE

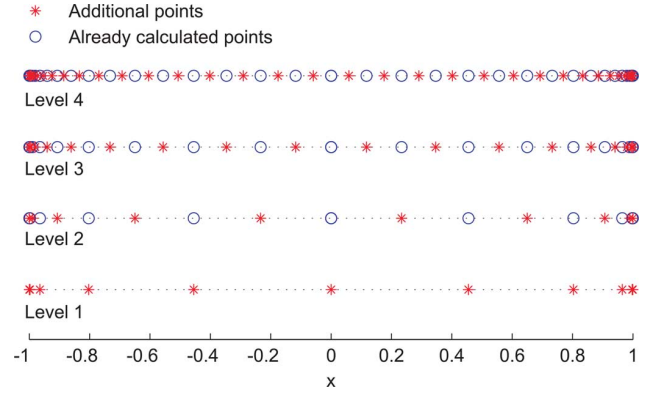


Fig. 3. Additional (stars) and already evaluated (circles) points of a DE rule if the DE rule is implemented in an adaptive way.

quadrature rule is written as

$$I(h) = \sum_{k=-n_1}^{n_1} \frac{h \cosh(kh)}{\cosh^2(\sinh(kh))} f(\tanh(\sinh(kh))). \quad (24)$$

At the next level $N + 1$, the sampling distance is $h/2$ and is given by

$$\begin{aligned} I\left(\frac{h}{2}\right) &= \frac{1}{2} I(h) + \sum_{k=-n_2, \text{ odd}}^{n_2} \frac{\frac{h}{2} \cosh\left(k \frac{h}{2}\right)}{\cosh^2\left(\sinh\left(k \frac{h}{2}\right)\right)} \\ &\quad \times f\left(\tanh\left(\sinh\left(k \frac{h}{2}\right)\right)\right) \end{aligned} \quad (25)$$

where the result of the previous step (24) has been reused in (25), and approximately only half of the quadrature points need to be calculated for the level $N + 1$. This results in almost halving the computational time when increasing the order of the DE quadrature rule. This property is visualized in Fig. 3, where, for each new level of the DE rule, only the red points need to be calculated [40].

B. Error Estimation for DE Rules

Advanced numerical modeling requires not only the value of the numerical integration but also an estimation of the error of the calculations. Then, the predefined level of accuracy can be obtained by automatically selecting the necessary number of integration points. The success of an error estimator lies in two main factors: their accuracy and the additional computational complexity required for their calculation.

An error estimator for quadratures based on trapezoidal discretization can be found in [45]. This error estimator can also be applied in the case of the DE as shown in [40]

$$E_{DE}(h) = \frac{h^3}{(2\pi)^2} \sum_{m=-n}^n \mathcal{D}^2 g(mh), \quad (26)$$

where \mathcal{D} denotes the differentiation operator and g is defined in (20). One of the advantages of this error estimator is that the additional computational effort lies in analytical derivations of the input function $f(x)$ and their sampling at exactly the same

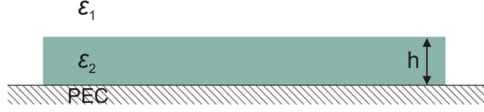


Fig. 4. Grounded dielectric slab.

points as the integration points of the DE rule. The differential operator \mathcal{D} is defined as follows:

$$\begin{aligned}\mathcal{D}^2 g(t) &= \mathcal{D}^2[f(\phi(t))\phi'(t)] \\ &= f(\phi(t))\phi_1(t) + f'(\phi(t))\phi_2(t) + f''(\phi(t))\phi_3(t)\end{aligned}\quad (27)$$

and $\phi_1(t) = \phi'''(t)$, $\phi_2(t) = 3\phi(t)\phi''(t)$ and $\phi_3(t) = [\phi'(t)]^3$. These calculations can be performed off-line, as the sampling points t and the functions $\phi_1(t)$, $\phi_2(t)$ and $\phi_3(t)$ are all known *a priori*. The additional computational cost to perform the error estimation resides in the calculation of $f'(\phi(t))$ and $f''(\phi(t))$, which, in the cases of (14) and (15), does not add excessive overhead, as will be shown in Section VI.

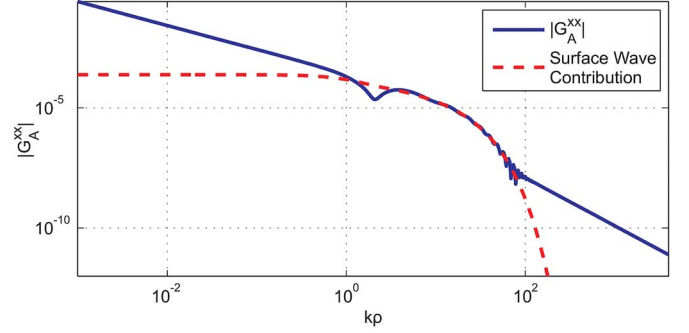
VI. NUMERICAL EXAMPLES

The validity and the performance of the aforementioned algorithms are demonstrated through three examples. The first one includes a dielectric slab backed by a PEC screen. Although no conductive sheet is present in this structure, this example illustrates the robustness of the method in a case where alternative techniques may fail. The second example introduces a graphene sheet where a plasmon mode propagates. The third example is a dielectric slab topped with a conductive sheet, which is a basic multilayered structure. All of the examples have been developed in the framework of the MPIE, and therefore various components of the vector potential GF are shown, alongside with the computational time required for their numerical evaluation.

A. Lossy Dielectric Slab

As a first benchmark to check the validity and the performance of the proposed methods, we choose the following multilayered structure: a lossy dielectric with $\varepsilon_{r2} = 4.4 - j0.352$ and thickness $h = 10$ mm backed by a PEC screen and topped by the semi-infinite free space as shown in Fig. 4.

The operating frequency of a horizontal source located on the interface between the lossy dielectric and the air is 10 GHz. In this example we focus on the computation of G_A^{xx} , which in general has only TE poles, if any, depending on the operating frequency and the characteristics of the slab. The observation point is also placed on the interface because this is the most challenging computational case for Sommerfeld integrals, as in this case there is no exponential attenuation in spectral domain GF. This specific example has received remarkable attention within the CEM community [11], [46] and has been considered as a benchmark for numerical methods dealing with Sommerfeld integrations. It has poles in the complex plane; indeed, a TE surface wave pole exists at $k_{\rho 1}^{\text{TE}} = (1.7418 - j0.0909)k$. The losses of the dielectric do not allow the assumption that after some wavelengths of horizontal separation between the source

Fig. 5. Spatial domain G_A^{xx} for the structure shown in Fig. 4. The contribution of the TE surface wave pole is also indicated.

and the observer the surface wave pole contribution is the dominant one, as quite fast the losses force a $1/\rho^2$ decay, as shown in Fig. 5, where the vector potential G_A^{xx} is plotted, alongside with the contribution of the surface wave pole. As already stated in [11], the surface wave contribution will become dominant only within a certain range of horizontal distances.

This example is a testcase where the classical complex image method (CIM) [47] fails. Different approaches have been proposed to overcome this issue. In [46], the CIM is combined with an imaginary axis integration of the Sommerfeld integral [12] in order to derive the spatial-domain GFs for moderate horizontal distances of some wavelengths. Alternatively, a special three-level DCIM approach was proposed [11] in order to enhance the efficiency of CIM and finally be able to numerically handle the situation of Fig. 4. However, these methods do not guarantee controllable and increased accuracy of the results, which is an inherent issue of the CIM. An initial attempt to relate the fitting error of the CIM in the spectral domain to the related one in the spatial domain was addressed in [48], increasing expectations for further improvements of the method.

The exactly same geometry is solved utilizing the proposed method based on the combination of the DE and WA algorithms for different levels of relative accuracy, varying from low to machine precision values. The results are shown in Fig. 6, where the thin dashed lines show the different predefined relative errors in terms of absolute error for different horizontal distances ρ .

Another purpose of Fig. 6 is to focus on the importance of the relative error of the calculations. Therefore, the relative error barrier is defined from $1e-4$ to $1e-12$. As the horizontal distance between source and observation points ρ increases, the value of the spatial domain GF is getting smaller. If a relative error of $1e-4$ is requested for the performed calculations, then the absolute error needs to remain below the first from the top thin dashed line, if the request is for a relative error of $1e-6$, the absolute error needs to be lower than the second thin dashed line, and so on.

The error for the first part of the Sommerfeld Integral was calculated with the method presented in Section V-B, while the error in the evaluation of the Sommerfeld tail was based on two consecutive converged partial integration steps. The thick dashed lines show the true absolute error of these calculations when compared with a reference solution, which is

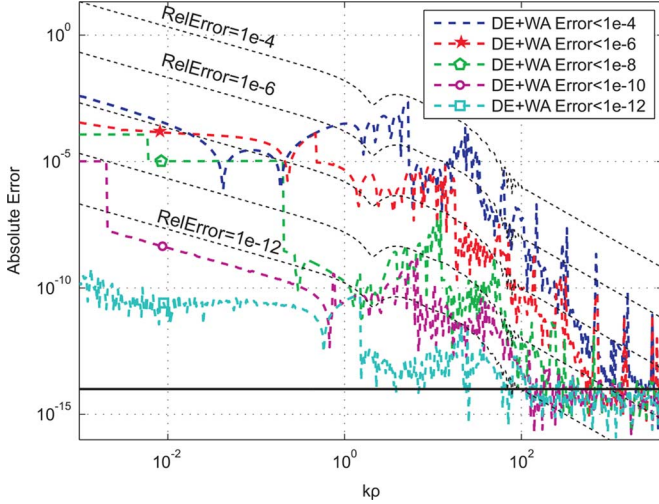


Fig. 6. Absolute error of G_A^{xx} of the proposed method for the structure shown in Fig. 4 for different levels of predefined relative error.

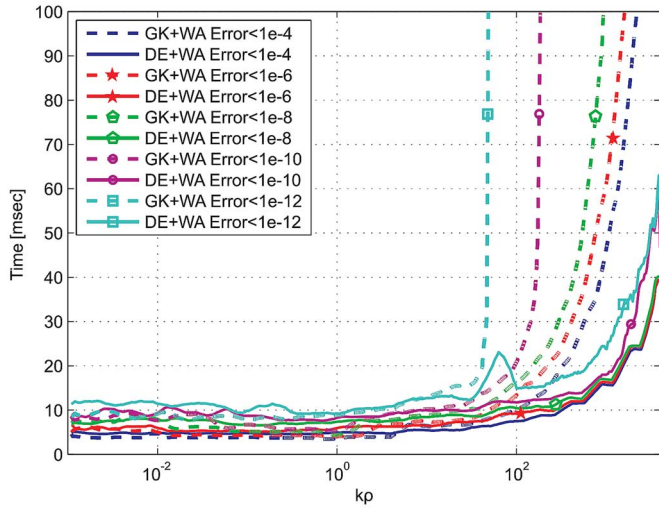


Fig. 7. Computational times of the proposed DE and WA algorithm (solid lines) and the reference detour and WA method (dashed lines) for different levels of predefined relative error for G_A^{xx} for the structure shown in Fig. 4.

obtained using as many integration points as necessary such that no change is observed until the 13th significant digit. The additional solid line indicates the numerical limit for double precision arithmetics.

The comparison concerning the computational time of the proposed method against the detoured integration [28] which is used as a reference method in this work is shown in Fig. 7.

The very precise error estimation was already observed in the trivial case of the free space GF [40], and a similar behavior is also observed in this far more complicated structure. The example shown in Fig. 7 includes both the DE and the WA algorithm calculations, thus accounting for the total time to compute the spatial-domain GF. For short horizontal separations ρ between the source and the observation points, the main contribution to the Sommerfeld integral is due to the tail. Therefore, the value of the first part of the Sommerfeld integral is smaller compared with the one of the tail and, in order to guarantee a predefined accuracy for the whole Sommerfeld integral, a much

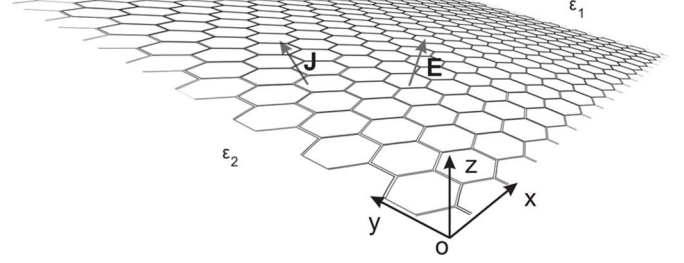


Fig. 8. Single graphene layer embedded in free space at the position $z = 0$.

higher relative accuracy is required for the tail than for the first part. For low accuracy and therefore for small values of ρ , both detoured and on-the-axis integration techniques perform almost equivalently. As the horizontal distance increases, the proposed method outperforms the reference one, which, for even moderately relative accuracies, fails.

However, even for low values of ρ , the proposed method is faster than the detoured one. The reason for this is that the calculation of the tail can start at a lower value of ξ_0 than in the detoured method, where we need to be sure that $\xi_0 > \max\{\text{real}(k_\rho)\}$. This fact is highlighted more in cases of high-permittivity layers or in plasmons, where the poles can be located far away from the branch point. A representative example of this case is shown in the following Subsection.

Comparing with methods belonging to CIM family, similar results to Fig. 5 have been obtained using the three-level DCIM method [11] within shorter computational times but sacrificing the guaranteed numerical accuracy.

B. Graphene Sheet

As a second demonstration, an example of high technological impact is selected. This is a graphene layer without a magnetic bias separating two semi-infinite media, as shown in Fig. 8. This example is important as it can support plasmon modes in the THz region, and its dyadic GFs for the fields have been developed [29], [49] using different approaches than the one proposed in this paper. More details on this example can also be found in [20].

Applying the strategy described in Section II, the scalar and vector potential spectral domain GFs can be derived. For demonstration purposes, the zx component of the dyadic GF for the vector potential A is hereby presented. If the source and observation points are assumed to be on opposite sides of the graphene layer, \tilde{G}_A^{zx} is given by

$$\tilde{G}_A^{zx} = -j\mu_0 e^{jk_{z2}z} e^{-jk_{z1}z'} \frac{k_x}{k_\rho^2} \frac{2k_{z2}D^{\text{TM}} + \varepsilon_2 k_{z1}D^{\text{TE}}}{D^{\text{TM}}D^{\text{TE}}} \quad (28)$$

where the TM and TE poles are given by

$$D^{\text{TM}}(\sigma) = k_{z1}k_{z2} \frac{\sigma}{\omega} + \varepsilon_2 k_{z1} + \varepsilon_1 k_{z2} \quad (29a)$$

$$D^{\text{TE}}(\sigma) = k_{z1} + k_{z2} + \mu_0 \sigma \omega \quad (29b)$$

and z' and z correspond to the vertical coordinate of the source and observation point, respectively. In the case that the conductivity of the sheet is described by a tensor instead of a scalar

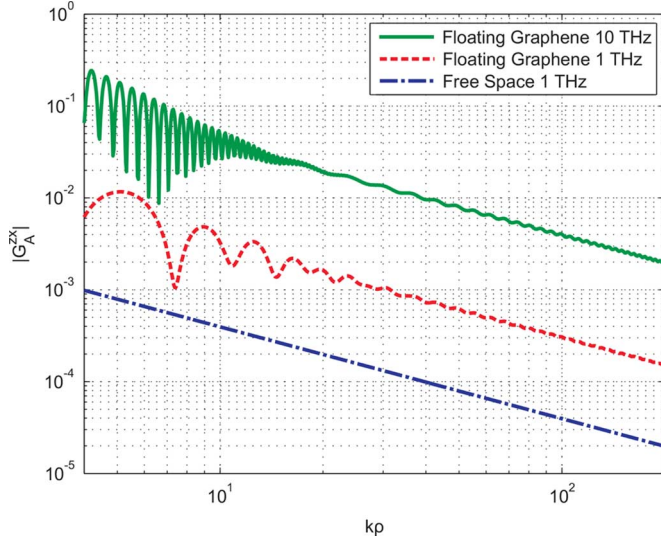


Fig. 9. $|G_A^{zx}|$ of floating graphene sheet for different horizontal distances ρ and frequencies. Source and observation points are located on the graphene sheet but on different sides.

value, the TM and TE poles are coupled, resulting in a hybrid mode

$$D^{\text{TM,TE}}(\vec{\rho}) = D^{\text{TM}}(\sigma_{uu})D^{\text{TE}}(\sigma_{vv}) - k_{z1}k_{z2}\mu_0\sigma_{uv}\sigma_{vu}. \quad (30)$$

The spatial-domain counterpart of \tilde{G}_A^{zx} has been calculated using the techniques described in Section III. It is plotted for $z' = z = 0$, which is the worst situation in terms of numerical complexity as (28) does not decay exponentially for large values of k_ρ . The results, where the two semi-infinite media are of the same dielectric ε_0 , are shown in Fig. 9 for different excitation frequencies and horizontal distances ρ .

The surface conductivity of graphene is estimated through the Kubo formula [50] at 300 K with a chemical potential of 0.2 eV and relaxation time of 1 ps. The behavior of a horizontal dipole in the cases of Fig. 9 radiating without the presence of the conductive sheet is also shown. The effect of the oscillations in the presence of graphene are due to the propagation of the plasmon mode, which, after some wavelengths, vanishes due to the high losses that it exhibits. Therefore, a behavior close to the free space one is retrieved.

Similarly to Fig. 4, the total computational time for the calculation of G_A^{zx} is shown in Fig. 10 when the excitation frequency is 10 THz. Different levels of accuracy have been predefined, and it becomes clear that for higher accuracies and horizontal distances between the source and the observation point, the proposed method outperforms the reference method that is the detoured integration [28]. It should be mentioned that all of the numerical examples were executed through MATLAB 7.12.0 (R2011a) in a single core of a Q9550@2.83 GHz processor. The `quadgk` routine, which is a vectorized adaptive implementation of a Gauss–Kronrod (GK) quadrature that is considered one of the fastest integration routines [51], was used for calculating the implementation time for the detoured method.

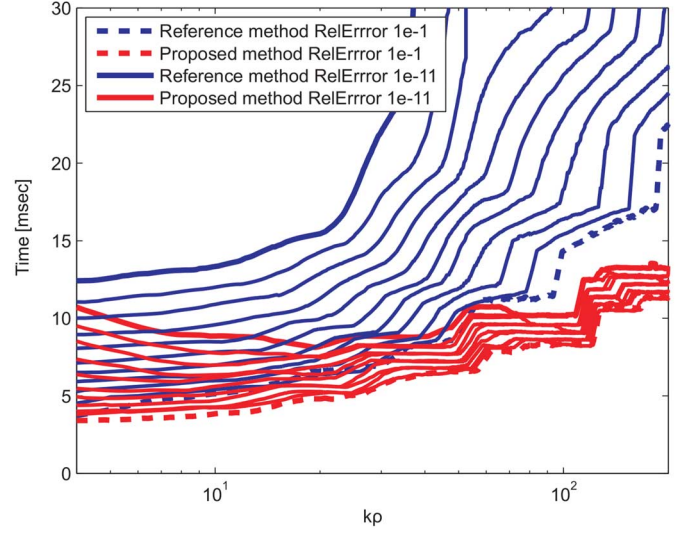


Fig. 10. Computational time for the Sommerfeld integral of (28) using the detoured integration and the WA algorithm as the reference method and the DE and WA algorithms in the proposed method.



Fig. 11. Grounded dielectric slab topped by a conductive sheet.

C. Grounded Slabs

A big family of multilayered structures that has been widely analyzed and used is the grounded slab. In general, it comprises a dielectric slab of finite thickness with metallization on one side. In this regard, three different types of grounded slabs can be defined. The first one, when the conductivity of the sheet σ tends to 0, is the classical grounded slab which serves as the substrate for a patch antenna. TM and/or TE surface waves may be supported depending on the parameters of the slab and the operating frequency. The second type is a grounded slab which is topped by a conductive sheet, as shown in Fig. 11. If the conductivity of this sheet is assumed to be real valued, then it becomes the basic design of a solar antenna [4]. Also, in this case, only TM and/or TE surface waves can be supported. If the conductivity becomes imaginary, typically if the metallic sheet is a graphene layer, then apart from the TM/TE surface waves a surface plasmon mode will also be present [52]. Finally, if the conductivity is tensorial, then hybrid TM/TE modes will be present.

If the top side of the slab is covered by a metallic layer as in Fig. 11, the design of a solar antenna is retrieved. This is a very useful design for satellites because a solar panel and an antenna can share the same surface. However, the presence of conductive layers on the top of the antenna will affect its performance, therefore the solar antenna has to be designed very carefully. In the range of operating frequencies of such antennas, the solar panel metallic sheets can be considered as very thin [4], [53]. A very accurate simulation of such structures can be performed using the methods described in the previous sections.

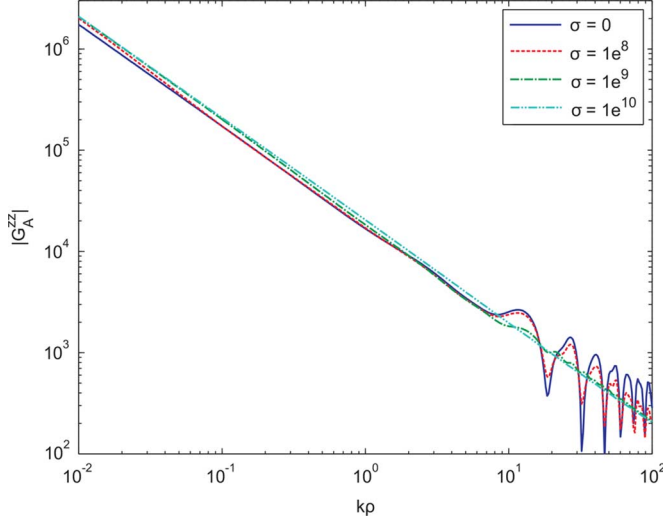


Fig. 12. G_A^{zz} of the grounded slab of Fig. 11 with $\varepsilon_2 = 5$ and thickness $h = \lambda$ at 1 THz topped by a sheet with a surface conductivity varying from 0 to very large values. Source and observation are on the top side of the conductive sheet.

Based on the Propagator Matrix, presented in Section II, the TM and TE poles for this specific structure can be found as

$$D_{\text{slab}}^{\text{TM}}(\sigma) = k_{z1}\varepsilon_2 + j \left(k_{z1}k_{z2}\frac{\sigma}{\omega} + \varepsilon_1k_{z2} \right) \tan(k_{z2}h) \quad (31a)$$

$$D_{\text{slab}}^{\text{TE}}(\sigma) = k_{z2} + j (k_{z1} + \mu_0\sigma\omega) \tan(k_{z2}h). \quad (31b)$$

Similarly to the classical grounded dielectric slab, the subindices 1 and 2 refer to the semi-infinite medium and the substrate, respectively, and h represents the slab's thickness. It is easy to verify from (31) that, if $\sigma \rightarrow 0$, the poles of the classical dielectric slab [5] can be retrieved.

If the source is placed on the top of the conductive sheet (assumed to be at $z_0 = 0$), then the vertical vector potential G_A^{zz} of the spectral domain GF for $z > z_0$ is found to be

$$\tilde{G}_A^{zz} = \frac{-j \varepsilon_2 k_{z1} + j k_{z1} k_{z2} \frac{\sigma}{\omega} \tanh(k_{z2}h)}{k_{z1} D_{\text{slab}}^{\text{TM}}(\sigma)} e^{-jk_{z1}z}. \quad (32)$$

The other components of the spectral-domain mixed potential GFs can also be derived in a straightforward way [24]. However, their analytical forms are lengthy and complicated and will be omitted here for clarity reasons.

As an example, the grounded slab of Fig. 11 with thickness $h = \lambda$ and permittivity $\varepsilon_2 = 5$ is topped by a metallic sheet whose conductivity varies. A vertical electric dipole, oscillating at 1 THz is placed on the top of the metallic sheet. The vertical vector potential G_A^{zz} is calculated for different horizontal distances ρ on the top of the sheet, as shown in Fig. 12.

Under the condition that the conductivity of the sheet is sufficiently large, e.g., $\sigma = 1e10$ S, the interface between the semi-infinite medium and the slab behaves like a PEC, and the GF of a dipole in free space is retrieved (with double strength due to the image theory). If the conductivity vanishes, then the solutions of the dielectric slab are derived, with the surface waves being dominant in larger horizontal distances. If the conductivity varies between these limiting cases, a mixed behavior is obtained with surface waves present.

Concerning the time comparison between the detoured path and the proposed one, the results are very similar to the one of

Fig. 7 and will be omitted due to space constraints. The reason for bearing such a similarity is that the position of the poles in the two structures, in Figs. 4 and 11, respectively, results in almost the same choice for ξ_0 . Only in the first case the imaginary part of the pole is due to the losses in the substrate, whereas in the second case it is due to the finite conductivity of the sheet.

VII. CONCLUSION

A general purpose technique for deriving the spectral-domain GFs including the vector and scalar potentials has been developed for structures with stacked dielectrics separated by conductive sheets with either scalar or tensorial description of their conductivity. Additionally, a novel and efficient integration technique has been presented for the error-controlled Sommerfeld integration of these GFs. The calculated spatial-domain GFs can serve as input to a MPIE code for the EM simulation of complex multilayered structures with conductive interfaces. If the difficulty of localizing the poles of the spectral-domain GFs for multilayered structures with an arbitrary number of sheets with tensorial conductivity is alleviated, then the proposed methods will perform equally well without any modification.

ACKNOWLEDGMENT

The authors would like to thank Dr. A. G. Polimeridis for his valuable help through fruitful discussions and excellent ideas.

REFERENCES

- [1] A. Vakil and N. Engheta, "Transformation optics using graphene," *Science*, vol. 332, no. 6035, pp. 1291–1294, 2011.
- [2] M. Tamagnone, J. S. Gómez-Díaz, J. R. Mosig, and J. Perruisseau-Carrier, "Reconfigurable THz plasmonic antenna concept using a graphene stack," *Appl. Phys. Lett.*, vol. 101, 2012, Art. ID 214102.
- [3] F. H. L. Koppens, D. E. Chang, and F. J. Garcia de Abajo, "Graphene plasmonics: A platform for strong light-matter interactions," *Nano Letters*, vol. 11, no. 8, pp. 3370–3377, 2011.
- [4] S. Vaccaro, J. R. Mosig, and P. de Maagt, "Two advanced solar antenna "solant" designs for satellite and terrestrial communications," *IEEE Trans. Antennas Propag.*, vol. 51, no. 8, pp. 2028–2034, Aug. 2003.
- [5] J. R. Mosig, R. C. Hall, and F. E. Gardiol, J. James and Hall, Eds., "Numerical analysis of microstrip patch antennas," in *Handbook of Microstrip Antennas*. London, U.K.: IEE-Peter Peregrinus, 1989.
- [6] T. Kaifas, "Direct rational function fitting method for accurate evaluation of sommerfeld integrals in stratified media," *IEEE Trans. Antennas Propag.*, vol. 60, no. 1, pp. 282–291, Jan. 2012.
- [7] Y. P. Chen, W. C. Chew, and L. Jiang, "A novel implementation of discrete complex image method for layered medium Green's function," *IEEE Antennas Wireless Propag. Lett.*, vol. 10, pp. 419–422, 2011.
- [8] H. Rogier, "New series expansions for the 3-D Green's function of multilayered media with 1-D periodicity based on perfectly matched layers," *IEEE Trans. Microw. Theory Techn.*, vol. 55, no. 8, pp. 1730–1738, Aug. 2007.
- [9] V. Okhmatovski and A. Cangellaris, "Evaluation of layered media Green's functions via rational function fitting," *IEEE Microw. Wireless Compon. Lett.*, vol. 14, no. 1, pp. 22–24, Jan. 2004.
- [10] R. Boix, A. Fructos, and F. Mesa, "Closed-form uniform asymptotic expansions of Green's functions in layered media," *IEEE Trans. Antennas Propag.*, vol. 58, no. 9, pp. 2934–2945, Sep. 2010.
- [11] A. Alparslan, M. I. Aksun, and K. A. Michalski, "Closed-form Green's functions in planar layered media for all ranges and materials," *IEEE Trans. Microw. Theory Techn.*, vol. 58, no. 3, pp. 602–613, Mar. 2010.
- [12] J. R. Mosig and A. Álvarez-Melcón, "Green's functions in lossy layered media: Integration along the imaginary axis and asymptotic behavior," *IEEE Trans. Antennas Propag.*, vol. 51, no. 12, pp. 3200–3208, Dec. 2003.

- [13] J. R. Mosig, "The weighted averages algorithm revisited," *IEEE Trans. Antennas Propag.*, vol. 60, no. 4, pp. 2011–2018, Apr. 2012.
- [14] K. A. Michalski, "Extrapolation methods for Sommerfeld integral tails," *IEEE Trans. Antennas Propag.*, vol. 46, no. 10, pp. 1405–1418, Oct. 1998.
- [15] R. Golubović-Nićiforović, A. G. Polimeridis, and J. R. Mosig, "Fast computation of Sommerfeld integral tails via direct integration based on double exponential-type quadrature formulas," *IEEE Trans. Antennas Propag.*, vol. 59, no. 2, pp. 694–699, Feb. 2011.
- [16] R. Golubović, A. G. Polimeridis, and J. R. Mosig, "Efficient algorithms for computing Sommerfeld integral tails," *IEEE Trans. Antennas Propag.*, vol. 60, no. 5, pp. 2409–2417, 2012.
- [17] P. Atkins and W. C. Chew, "Fast computation of the dyadic Green's function for layered media via interpolation," *IEEE Antennas Wireless Propag. Lett.*, vol. 9, pp. 493–496, 2010.
- [18] K. Yang and A. Yilmaz, "A three-dimensional adaptive integral method for scattering from structures embedded in layered media," *IEEE Trans. Geosci. Remote Sens.*, vol. 50, no. 4, pp. 1130–1139, Apr. 2012.
- [19] V. Okhmatovski, M. Yuan, I. Jeffrey, and R. Phelps, "A three-dimensional precorrected FFT algorithm for fast method of moments solutions of the mixed-potential integral equation in layered media," *IEEE Trans. Microw. Theory Techn.*, vol. 57, no. 12, pp. 3505–3517, Dec. 2009.
- [20] I. D. Koufogiannis, M. Mattes, and J. R. Mosig, "On the development and evaluation of spatial domain green functions for multilayered structures with conductive sheets," in *Proc. IEEE MTT-S Int. Conf. Numer. Electromagn. Modeling and Optimization for RF, Microw., and Terahertz Applic.*, Pavia, Italy, 2014.
- [21] L. B. Felsen and N. Marcuvitz, *Radiation and Scattering of Waves*. New York, NY, USA: IEEE, 1994.
- [22] K. A. Michalski and J. R. Mosig, "Multilayered media Green's functions in integral equation formulations," *IEEE Trans. Antennas Propag.*, vol. 45, no. 3, pp. 508–519, Mar. 1997.
- [23] K. Michalski and D. Zheng, "Electromagnetic scattering and radiation by surfaces of arbitrary shape in layered media. I. Theory," *IEEE Trans. Antennas Propag.*, vol. 38, no. 3, pp. 335–344, Mar. 1990.
- [24] T. M. Grzegorzczuk and J. Mosig, "Full-wave analysis of antennas containing horizontal and vertical metallizations embedded in planar multilayered media," *IEEE Trans. Antennas Propag.*, vol. 51, no. 11, pp. 3047–3054, Nov. 2003.
- [25] I. D. Koufogiannis, M. Mattes, and J. R. Mosig, "Mixed potentials for planar multilayered structures including conductive interfaces," in *Proc. 8th Eur. Conf. Antennas Propag.*, 2014, pp. 1522–1524.
- [26] A. Sommerfeld, *Partial Differential Equations in Physics*. New York, NY, USA: Academic, 1949.
- [27] I. S. Gradshteyn and I. M. Ryzhik, A. Jeffrey and D. Zwillinger, Eds., *Table of Integrals, Series, and Products*, 7th ed. Amsterdam, The Netherlands: Elsevier, 2007.
- [28] P. Gay-Balmaz and J. R. Mosig, "Three-dimensional planar radiating structures in stratified media," *Int. J. Microw. Millimeter-Wave Comput.-Aided Eng.*, vol. 7, no. 5, pp. 330–343, 1997.
- [29] A. Nikitin, F. Garcia-Vidal, and L. Martin-Moreno, "Analytical expressions for the electromagnetic dyadic Green's function in graphene and thin layers," *IEEE J. Sel. Topics Quantum Electron.*, vol. PP, no. 99, p. 1, 2012.
- [30] A. G. Polimeridis, T. V. Yioultsis, and T. D. Tsioboukis, "An efficient pole extraction technique for the computation of Green's functions in stratified media using a sine transformation," *IEEE Trans. Antennas Propag.*, vol. 55, no. 1, pp. 227–229, Jan. 2007.
- [31] H. Rogier and D. Vande Ginste, "A fast procedure to accurately determine leaky modes in multilayered planar dielectric substrates," *IEEE Trans. Microw. Theory Techn.*, vol. 56, no. 6, pp. 1413–1422, Jun. 2008.
- [32] L. Knockaert, H. Rogier, and D. D. Zutter, "An FFT-based signal identification approach for obtaining the propagation constants of the leaky modes in layered media," *Int. J. Electron. Commun.*, vol. 59, no. 4, pp. 230–238, 2005.
- [33] J. Ding and S. Dvorak, "An accurate and systematic surface-wave pole location method for multilayered media," *IEEE Trans. Antennas Propag.*, vol. 62, no. 2, pp. 997–1001, Feb. 2014.
- [34] Z. Song, H.-X. Zhou, K.-L. Zheng, J. Hu, W.-D. Li, and W. Hong, "Accurate evaluation of Green's functions for a lossy layered medium by fast extraction of surface-and leaky-wave modes," *IEEE Antennas Propag. Mag.*, vol. 55, no. 1, pp. 92–102, Feb. 2013.
- [35] F. Demuynck, G. Vandenbosch, and A. Van de Capelle, "The expansion wave concept. I. Efficient calculation of spatial Green's functions in a stratified dielectric medium," *IEEE Trans. Antennas Propag.*, vol. 46, no. 3, pp. 397–406, 1998.
- [36] A. K. Abdelmaged and A. A. K. Mohsen, "An accurate computation of Green's functions for multilayered media in the near-field region," *Microw. Opt. Technol. Lett.*, vol. 29, no. 2, pp. 130–131, 2001.
- [37] E. Simsek, Q. H. Liu, and B. Wei, "Singularity subtraction for evaluation of Green's functions for multilayer media," *IEEE Trans. Microw. Theory Techn.*, vol. 54, no. 1, pp. 216–225, Jan. 2006.
- [38] A. G. Polimeridis and J. R. Mosig, "Evaluation of weakly singular integrals via generalized Cartesian product rules based on the double exponential formula," *IEEE Trans. Antennas Propag.*, vol. 58, no. 6, pp. 3011–3019, Jun. 2010.
- [39] H. Takahasi and M. Mori, "Double exponential formulas for numerical integration," *Kyoto Univ. Publ. RIMS*, no. 9, pp. 721–741, 1974.
- [40] I. D. Koufogiannis, A. G. Polimeridis, M. Mattes, and J. R. Mosig, "Real axis integration of Sommerfeld integrals with error estimation," in *Proc. 6th Eur. Conf. Antennas Propag.*, 2012, pp. 719–723.
- [41] H. Takahasi and M. Mori, "Estimation of errors in the numerical quadrature of analytic functions," *Applicable Anal.*, vol. 1, no. 3, pp. 201–229, 1971.
- [42] M. Mori, "Discovery of the double exponential transformation and its developments," *Kyoto Univ. Publ. RIMS*, no. 41, pp. 897–935, 2005.
- [43] D. H. Bailey, K. Jeyabalan, and X. S. Li, "A comparison of three high-precision quadrature schemes," *Exper. Math.*, vol. 3, no. 14, pp. 317–329, 2005.
- [44] I. D. Koufogiannis, A. G. Polimeridis, M. Mattes, and J. R. Mosig, "A parametric study of the double exponential algorithm utilized in weakly singular integrals," in *Proc. 5th Eur. Conf. Antennas Propag.*, 2011, pp. 2147–2151.
- [45] D. H. Bailey and J. M. Borwein, "Effective error bounds in Euler-Maclaurin-based quadrature schemes," in *Proc. Conf. High-Performance Computing Syst.*, 2006, p. 34.
- [46] N. Shuley, R. Boix, F. Medina, and M. Horno, "On the fast approximation of Green's functions in MPIE formulations for planar layered media," *IEEE Trans. Microw. Theory Techn.*, vol. 50, no. 9, pp. 2185–2192, Sep. 2002.
- [47] M. Aksun, "A robust approach for the derivation of closed-form Green's functions," *IEEE Trans. Microw. Theory Techn.*, vol. 44, no. 5, pp. 651–658, May 1996.
- [48] E. Karabulut, A. T. Erdogan, and M. Aksun, "Discrete complex image method with spatial error criterion," *IEEE Trans. Microw. Theory Techn.*, vol. 59, no. 4, pp. 793–802, Apr. 2011.
- [49] G. Lovat, "Equivalent circuit for electromagnetic interaction and transmission through graphene sheets," *IEEE Trans. Electromagn. Compat.*, vol. 54, no. 1, pp. 101–109, 2012.
- [50] L. A. Falkovsky, "Optical properties of graphene," *J. Phys., Conf. Series*, vol. 129, no. 1, 2008, Art. ID 012004.
- [51] L. F. Shampine, "Vectorized adaptive quadrature in Matlab," *J. Comput. Appl. Math.*, vol. 211, Feb. 2008.
- [52] G. W. Hanson, E. Forati, W. Linz, and A. B. Yakovlev, "Excitation of terahertz surface plasmons on graphene surfaces by an elementary dipole and quantum emitter: Strong electrodynamic effect of dielectric support," *Phys. Rev. B*, vol. 86, Dec. 2012, Art. ID 235440.
- [53] S. Vaccaro, P. Torres, J. R. Mosig, A. Shah, J.-F. Zürcher, A. Skrivervik, F. Gardiol, P. de Maagt, and L. Gerlach, "Integrated solar panel antennas," *Electron. Lett.*, vol. 36, no. 5, pp. 390–391, 2000.

Ioannis D. Koufogiannis (M'14), photograph and biography not available at the time of publication.

Michael Mattes (M'08), photograph and biography not available at the time of publication.

Juan R. Mosig (F'99), photograph and biography not available at the time of publication.